Ring buckling and C=N isomerization pathways for efficient photoprotection in two nature-inspired UVA sunscreens revealed through ultrafast dynamics and high-level calculations

Adam M. Cowden[1,2] | Raúl Losantos[3] | Abigail L. Whittock[1,4] | Beatriz Peñín[3] |
Diego Sampedro[3] | Vasilios G. Stavros[1,5]

[1]Department of Chemistry, University of Warwick, Coventry, UK

[2]Molecular Analytical Science Centre for Doctoral Training, Senate House, University of Warwick, Coventry, UK

[3]Departamento de Química, Centro de Investigación en Síntesis Química (CISQ), Universidad de La Rioja, Logroño, Spain

[4]Analytical Science Centre for Doctoral Training, Senate House, University of Warwick, Coventry, UK

[5]School of Chemistry, University of Birmingham, Edgbaston, Birmingham, UK

Correspondence
Diego Sampedro, Departamento de Química, Centro de Investigación en Síntesis Química (CISQ), Universidad de La Rioja, Madre de Dios, 53, 26006 Logroño, La Rioja, Spain.
Email: diego.sampedro@unirioja.es

Vasilios G. Stavros, Department of Chemistry, University of Warwick, Gibbet Hill Road, Coventry CV4 7AL, UK and School of Chemistry, University of Birmingham, Edgbaston, Birmingham B15 2TT, UK.
Email: v.stavros@warwick.ac.uk and v.stavros@bham.ac.uk

Abstract

Sunscreens provide a frontline defense for our DNA against the damage caused by ultraviolet (UV) radiation. The active ingredients in topically applied sunscreens that provide this defense are UV filters, which preferentially absorb or reflect UV radiation before it penetrates the skin and interacts with photosensitive nucleic acids. However, there are concerns related to human and environmental toxicity of current UV filters, and consequently a shift toward nature-inspired, particularly microbial, UV filters. In this paper, new physical insight is provided into the fundamental mechanisms of photoprotection in two synthetic analogs of mycosporine-like amino acid-type UV filters, demonstrating new methods of protection that are distinct from those of current commercial sunscreens, extending previous work in this area. Transient absorption measurements (both transient electronic absorption spectroscopy and transient vibrational absorption spectroscopy) are combined with steady-state studies and high-level computational results to aid our mapping of the experimentally derived lifetimes to real-time photodynamic processes. The conclusions reached here pave the way toward developing new and more efficient biomimetic DNA photoprotectant materials.

Abbreviation: AUC, area under curve; AUCI, area under curve index; CI, conical intersection; ESA, excited state absorption; GSB, ground state bleach; MAAs, mycosporine-like amino acids; TEAS, transient electronic absorption spectroscopy; TVAS, transient vibrational absorption spectroscopy; UV, ultraviolet.

Adam M. Cowden, Raúl Losantos and Abigail L. Whittock contributed equally to this work.

This article is part of a Special Issue dedicated to the topic of Nucleic Acid Photophysics.

INTRODUCTION

Researchers and sunscreen formulators are tasked with manufacturing a stable, well-characterized product that can protect consumers against the full UV spectrum of light that reaches the Earth's surface (290–400 nm wavelengths). UV is implicated in many deleterious processes in the human body, ranging from premature skin aging to carcinogenesis, and can be subdivided into lower energy UVA (320–400 nm) and higher energy UVB (290–320 nm).[1–3] While there is already a large pool of UVB filters available, there is a pressing need to develop UVA filters for broadband coverage.[4] UVA, at longer wavelengths to UVB, is abundant at Earth's surface level and is able to penetrate the surface of unprotected human skin and impart excess energy to DNA, leading to harmful downstream effects. These consequences can be significantly reduced by, for example, applying a topical barrier that reduces transmission.[5] The search for UVA filters has been under way for decades, yet the photoinstability of the contemporarily most widely used UVA absorbing compound, avobenzone, continues to raise concerns for our well-being as well as for the environment.[4,6–9] As dermatologists continue to encourage people to apply proper photoprotection, there is a call for novel and more effective compounds with better stability and safety profiles.[10] One productive line of investigation has been to draw compounds from nature's own bank of sunscreens with researchers already having identified compounds of particular interest from multiple natural sources such

as microbes, terrestrial plants, and the marine environment.[11,12] Such compounds are found in organisms living in locations with high levels of UV flux where they have presumably evolved life-sustaining photoprotection mechanisms over geological timescales[13,14]; recommending their tailored sunscreening molecules and pigments for adaptation by our chemical and cosmetics industries.

In this paper, we build on previous studies of the mechanism of photoprotection in synthetic analogs of mycosporine-like amino acids (MAAs), a family of secondary metabolites that are typically extracted from red seaweed and many other marine organisms; taking shinorine as a distinguishing example (Figure 1A).[15–17] Synthetic (i.e., made-in-the-lab) molecules that retain the photoprotective properties of MAAs could be produced routinely with chemical methods at greater scale than the natural products, providing a distinct advantage for scale-up. Indeed the more widespread use of MAAs as UV filters has so far been stymied by the low abundance of these molecules in their natural sources (typically up to 7 pg MAA cell^{-1} in microalgal cultures or ~10s of ng L^{-1} for individual MAAs in natural populations) as well as the complexity of extraction, purification, and separation.[18] The benefits of introducing a nature-inspired photoprotective library into a commercial sunscreen manufacture could mean increased long-term stability, improved biological compatibility, higher absorption coefficients, complementary antioxidant activity, and better safety profiles than the current state-of-the-art sunscreen molecules, based on seminal studies in MAAs and MAA-like molecules.[19–21]
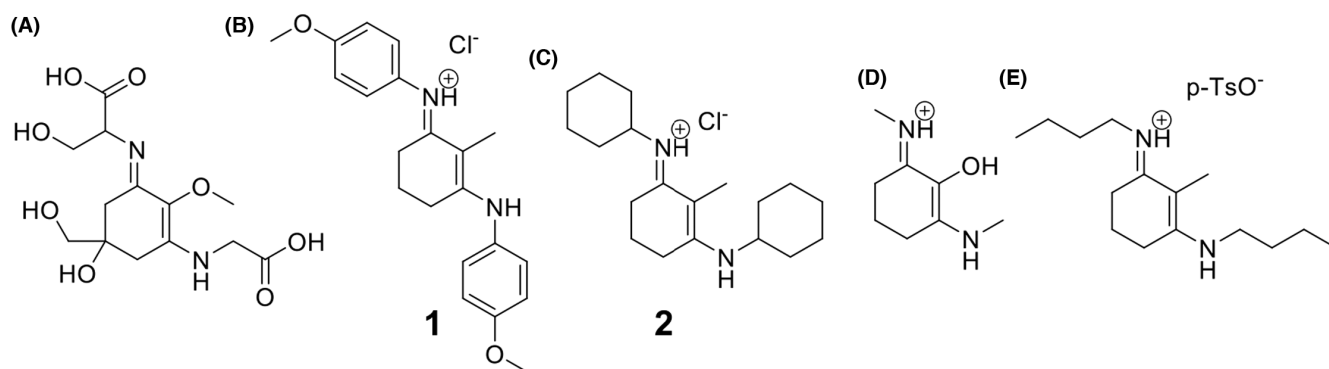
FIGURE 1 The chemical structures of (A) shinorine, (B) **1**, (C) **2**, (D) the cyclohexenimine core with N-methyl substituents studied in Ref. 26, (E) molecule studied in Ref. 32.

With the ability to use modern ultrafast spectroscopy to follow energy flux in real-time, a full understanding of the mechanism of excess energy dissipation after a molecule has been excited by interaction with light should increase the confidence of regulators, the compliance of consumers, and inform rational design of novel photoprotective materials in general.

An essential molecular scaffold of MAAs is the cyclic hexenimine core which is typically substituted through the nitrogen atom by chemical groups derived from an amino acid (see Figure 1). Based on a survey of a public domain database containing >70 MAA molecules, this family of molecules absorbs wavelengths between 309 and 362 nm with high extinction coefficients between 28,100 and ~50,000 $M^{-1} cm^{-1}$.[22] In terms of their ability to act as sunscreens, it is now established that after photon absorption MAAs readily dissipate excess energy as heat through intermolecular interactions with the surrounding medium, which is typically an aqueous or polar solvent or emulsion.[23,24] In an ideal sunscreen, processes that dissipate energy must occur as quickly as possible, allowing the molecule to return intact to its original ground state, thus freeing it to absorb another photon; and then to repeat the process ad infinitum. In general, efficient recovery of the ground state, in terms of energy and geometry, allows the molecules to retain UV screening potency over long periods of time while limiting the formation of photoproducts and avoiding undesirable photochemical reactions.[25]

In a computational study of MAA analogs, Losantos et al.[26,27] modeled using the complete active space second-order perturbation theory/complete active space self-consistent field (CASPT2//CASSCF) strategy, critical points along the reaction coordinate of energetically excited cyclic hexenimine cores as they lose energy. For a cyclic hexenimine core with N-methyl substituents (Figure 1D), a low-energy conical intersection (CI) connecting the first electronic excited state potential energy surface (S_1) with the electronic ground state (S_0) was reported[26]; concurring with the CI found in gadusol and the natural MAAs, palythine and porphyra-334.[28–31] A CI is a point between the energy surfaces where molecular population can freely traverse and it is a key checkpoint in relaxation processes. An out-of-plane movement (i.e., an aborted geometrical deformation between planar and non-planar forms of the molecule, herein referred to as "ring-buckling") was used to explain the photodynamic evolution toward the CI. Non-adiabatic molecular dynamics (NAMD) were used alongside to predict an excited state lifetime on the order of ~200 fs for this dynamic process.

The same researchers then reported, in a combined computational and experimental study, that a new CI had been found for a C=N photoisomerization coordinate when phenyl rings were substituted on the cyclic hexenimine core. Based on that study, it is now thought that MAA-like molecules with N-phenyl substituents evolve from the initially excited Franck-Condon geometry to the S_1/S_0 CI through an alternative relaxation process to natural MAAs and other analogs studied thus far.[27] Separately, Woolley and co-workers reported the intrinsic photoprotection of a related molecule with a cyclic hexenimine core and alkyl substituents with ultrafast experimental results (Figure 1E).[32] In their study, photoexcitation resulted in population of the first singlet electronic excited state (S_1) which is in line with the computational study of Losantos et al. cited above. The excited state population persisted for ~500 fs before populating the vibrationally hot electronic ground state (S_0), which then cooled slowly to the original S_0 ground state through vibrational relaxation. Similar results were also observed for natural MAAs.[16,33]

In summary, all studies on this class of molecules thus far have pointed to efficient internal conversion (IC) pathways that recommend their use as solar DNA photoprotectors, albeit with different underlying photodynamics that warrants further investigation.

In this paper, new physical insight is provided into the fundamental mechanisms of photoprotection in two MAA analogs. To support our analysis, we have combined transient absorption measurements (both transient electronic absorption spectroscopy [TEAS] and transient vibrational absorption spectroscopy [TVAS]) with steady-state studies and high-level computational results. Taken together, we can confidently explain the molecular movements underpinning the relaxation pathways and show that two distinct mechanisms are indeed at play as these two similar molecules are compared under the same conditions for the first time.

The two molecules chosen for this study (called **1** [Figure 1B] and **2** [Figure 1C]) are modeled on the MAA structure (exemplified by shinorine, Figure 1A) but differ in their N-substituents. The substituents were chosen to probe a new reaction channel that is available to compounds with phenyl substituents compared to other related compounds with non-aromatic substituents (e.g., methyl substituents).[27] The design rationale came about by considering the availability of starting materials for a simple one-step reaction that involves reacting cyclohexenones with secondary amines to produce cyclohexenimines, to make useful analogs of MAAs. Aromatic, secondary amines such as the para-OMe group used to produce **1**, and cycloalkyl amines such as the cyclohexylamine used in making **2** are readily available. It is worth adding that there are no known natural MAAs containing these groups so they are an interesting avenue to investigate, allowing us to use the "natural" N-C=C-C=N- motif in a synthetic setting. For the first time, a direct comparison

can be made between the two proposed mechanisms since both the cyclic hexenimine previously studied (molecule **1**) and new molecule **2** are studied under the same experimental conditions.

MATERIALS AND METHODS

Synthesis

Compounds **1** and **2** (Figure 1B,C) were prepared following a previously published general synthetic route.[26] To a suspension of the corresponding ketone precursor (1 mmol) in dry toluene (50 mL), p-toluenesulfonic acid monohydrate (1 mmol) was added. The mixture was stirred for 5 min at room temperature. The relevant amine (6 mmol) was added, and the mixture was refluxed for between 24 and 84 h. After cooling, the reaction mixture was concentrated under vacuum and was purified by recrystallization from dichloromethane and hexane. The tosylate counterion was exchanged with chloride using an Amberlite IRA-402-Cl ion-exchange resin to obtain the products as the chloride salts. **1** (IUPAC: 4-methoxy-N-(3-((3-methoxyphenyl)amino)-2-methylcyclohex-2-en-1-ylidene)benzenaminium chloride); **2** (IUPAC: N-(3-(cyclohexylamino)-2-methylcyclohex-2-en-1-ylidene)cyclohexanaminium chloride).

Steady-state spectroscopy

Long-term photostability data were obtained using samples of ~10-μM concentrations in absolute ethanol (VMR chemicals). To simulate the response under near-to-life conditions, irradiations were carried out using a solar simulator (LCS-100 model 94011A, Oriel Instruments; see Figure S1). Samples were prepared in quartz cuvettes (Hellma Analytica) of 10×10 mm pathlength containing 3 mL of each solution. The distance of the cuvette from the lamp was adjusted so that each sample was exposed to the power of the sun at Earth's surface (1000 W/m²).[34] Spectra were recorded on a UV-visible spectrometer (Cary 60, Agilent Technologies) at specified time intervals up to 2 h at a scan rate of 600 nm/min with 1-nm intervals. The critical wavelength of each compound was determined using the area under curve (AUC) function in OriginPro (Figure S2). Extinction coefficients (ε (M^{-1}cm^{-1})) were determined by a linear fit to a series of five concentrations for each molecule in ethanol at increasing concentrations (Figure S3). For the supplementary single wavelength irradiation study of **1**, a 341 nm beam with a bandwidth of 8 nm from a xenon arc lamp (Fluorolog 3, Horiba) was used and the power was adjusted with an ND filter to the

equivalent solar irradiance power at this wavelength and bandwidth. Fluorescence spectra were acquired for **1** and **2** using a spectrofluorometer (Fluorolog 3, Horiba) setup with an emission and excitation bandwidth of 2.5 nm; the excitation wavelength was 341 nm for **1** and 329 nm for **2**. Fluorescence quantum yields were measured using an FS5 spectrofluorometer (Edinburgh Instruments) fitted with an integrating sphere.

Ultrafast spectroscopy

Transient electronic absorption spectroscopy and TVAS measurements were performed at the Warwick Centre for Ultrafast Spectroscopy (WCUS: www.go.warwick.ac.uk/fac/sci/wcus). The TEAS setup has been previously reported by colleagues working in the facility and is therefore outlined here with pertinent details about the current experiment.[32] Ultrafast pulses were generated by a Ti:Sapphire oscillator with regenerative amplification to produce a fundamental 800-nm femtosecond laser pulse. This fundamental is initially split into four ways for each experiment table in WCUS and then into two beams for the pump and probe pulses of the TEAS experiment. The pump beam passes through an optical chopper operating at a repetition rate of 500 Hz, blocking every other pulse of the 1 kHz pulse train and allowing for direct comparison of the signal for the pumped and unpumped samples. Sample solutions of 1 mM in ethanol were continuously passed through a demountable liquid cell (Harrick Scientific Products Inc.) using a diaphragm pump (SIMDOS). To permit interaction with the incident light, the cell was fitted with CaF$_2$ windows and PTFE spacers (100 μm). The pump beam was tuned for each sample solution to the maximum absorbance wavelength (λ_{peak}) of each compound in ethanol (341 nm for **1** and 329 nm for **2**) using an optical parameter amplifier (Topas-Prime with UV extension, Light Conversion). The power of the pump beam at the sample was adjusted to ~500 μW and the pump and probe beams were spatially aligned at the sample holder. The pump beam diameter at the sample was ~400 μm. The probe pulse polarization was set to the magic angle, 54.7°, with respect to the pump pulse polarization. The probe beam white light continuum (300–720 nm) was generated by focusing a small portion of the 800 nm fundamental onto a vertically translating 2 mm CaF$_2$ window. The pathlength of the probe was adjusted to give pump-probe time delays (Δt) from −1 ps to 3 ns using a motorized optical delay stage with a mounted retroreflector. To enable determination of the change in optical density (ΔOD), the incident beam transmitted for the pumped sample (I) and incident beam transmitted for the unpumped

sample (I_0) were detected using a fiber-coupled spectrometer (AvaSpec-ULS1650F, Avantes). Averaged data are plotted as transient absorption spectra (TAS) in the form of false-color heat maps. The TAS has been chirp-corrected with the KOALA software package and fitted with a sequential kinetic model $\left(A \overset{\tau_1}{\to} B \overset{\tau_2}{\to} C \overset{\tau_3}{\to} \dots \right)$ using the software package Glotaran.[35–37]

For the TVAS setup, 10-mM solutions of **1** and **2** were circulated through a demountable liquid cell the same way as for the TEAS experiments. The method that has been previously reported by our group is adapted to this experiment.[38] The pump beam wavelengths and power were as used in the TEAS experiment (i.e., 341 nm for **1** and 329 nm for **2** at 500 μW). The probe beam was generated by seeding a second optical parametric amplifier (Topas-C, Spectra-Physics) with a second fraction of the fundamental 800 nm beam. The generated probe beam allows for a tuneable IR wavelength that includes 6288 and 6536 nm (the central wavelengths used for **1**) and 6456 nm (**2**). Two probe wavelengths were used for **1** due to oversaturation of the detector and these were stitched together to produce the final spectrum. The pathlength of the probe beam was varied in a similar way to the TEAS setup to allow time delays (Δt) of up to 1 ns. As in the TEAS experiment, the pump beam passes through an optical chopper operating at 500 Hz. Atmospheric absorption lines were excluded by purging the probe line with nitrogen gas. The probe pulse passes through the sample where it is partially absorbed before entering an imaging spectrometer (iHR320, HORIBA Scientific). Once in the spectrometer, the probe is dispersed by a diffraction grating (6 μm blaze, 100 lines mm^{-1} resolution) onto a mercury cadmium telluride (MCT) detector 64-pixel array (FPAS-0144, Infrared Systems Development). The MCT detector is cooled using liquid nitrogen to reduce thermal contributions to the signal. Pixel number is converted to wavenumber using a mid-IR polystyrene calibration card (Perkin Elmer) as reference. Bi-exponential fits of the GSB features in origin were employed to extract lifetimes associated with the dynamical processes following photoexcitation.

FTIR spectroscopy

Fourier-transform infrared spectra were recorded on a FTIR spectrometer (VERTEX 70v, Bruker) between 500 and 4000 cm^{-1} with 1 cm^{-1} resolution. A nitrogen environment was used to remove vibrational modes associated with atmospheric gases. A quantity of 10 mM solutions were contained within a demountable liquid cell (Harrick Scientific Products Inc.) with a pathlength of 100 μm. This was achieved by inserting 100-μm PTFE spacers between two CaF$_2$ windows (front window 1 mm and back window 2 mm thickness).

Computational methods

A series of on-the-fly non-adiabatic molecular dynamic (NAMD) calculations were carried out to analyze the deactivation process of compounds **1** and **2**. The CASSCF (6,5)/6-31G* level of theory[39] was used considering two roots: the ground state and the first excited state that exhibits a π-π* nature in both compounds. This method agrees with the behavior already observed for model compounds and corresponds to the excitation to the brightest state, i.e., the state that is populated experimentally. To ensure an accurate description of the deactivation process, Tully's fewest switches algorithm[40,41] was used as implemented in OpenMolcas version 20.10.[42,43] Calculations were performed in vacuum using a Nose-Hoover chain of thermostats with T = 298 K to maintain a constant temperature.[44,45] The active space for compound **1** was verified versus (14,13) including four π orbitals and their corresponding π* orbitals. Both potential energy surfaces feature identical properties, independently of the used active space.[27] The orbitals included in all the active spaces for **1** and **2** can be found in the ESI. Additionally, the comparison of both active spaces in the conical intersection geometry can be seen in Figures S15 and S16. The simplification of considering two roots for the dynamics is based on the high energy difference found with the next excited state (S$_2$) (being more than 1.5 eV), together with the need to decrease the computational cost as much as possible. The energy of the states found with four roots for **1** (14,13), **1** (6,5), and **2** (6,5) are presented in the ESI.

For initial conditions, a series of 50 geometries were generated by performing a Boltzmann distribution around the equilibrium geometry at 298 K, while also obtaining the respective velocities. Each trajectory was run for up to 800 fs for both **1** and **2**. Longer times were unreachable due to the high computational cost involved in this type of calculation. Trajectories and populations were analyzed using a series of homemade scripts. For the population analysis, an average of all trajectories was estimated considering the individual population at each time.

For the thermal MP2 study, PCM[46] was used to include ethanol effects at the MP2/6-31G* level of theory.[47,48] The calculations were done using Gaussian16[49] and the minima and TS verified by frequency calculations showing none and one imaginary frequency, respectively. The use of MP2 was chosen to provide an accurate geometrical description of the ground state, even though the dynamic electron correlation was not found to be critical.

RESULTS AND DISCUSSION

Experimental results

The compounds were prepared in a single reaction with good yield and a simple purification process, which are ideal features for their use in sunscreens at scale. The UV-visible absorption profiles as illustrated in Figure 2 span the UVA-UVB region and confirm that these molecules are absorbers of solar UV radiation. The extinction coefficients (ε (M^{-1}cm^{-1})) were determined at the respective absorption maxima as ~64,100 (**1**) and ~60,700 (**2**) in ethanol; and these values suggest that **1** and **2** are even stronger absorbers than the natural MAA molecules. Additionally, the critical wavelengths (λ_{crit}) of **1** and **2** in ethanol were determined to quantify the wavelength below which 90% of the absorption between 290 and 400 nm occurs. **1** has a λ_{crit} of 374 nm and **2** has a λ_{crit} of 344 nm (see Supporting Information). To claim broadband protection, the critical wavelength should be at least 370 nm, and thus **1** satisfies this condition while **2** does not.[50] According to the computed spectra, the major observed band of both **1** and **2** can be attributed to the $S_1 \leftarrow S_0$ transition which has $\pi\pi^*$ character, with other transitions occurring at considerably higher energy.[27]

An in vitro measurement of photostability is the percentage degradation of a molecule under the action of UV or solar light, and this can be quantified by Equation 1:

$$\% \, \text{decrease} = \frac{c_I - c_F}{c_I} \times 100. \qquad (1)$$
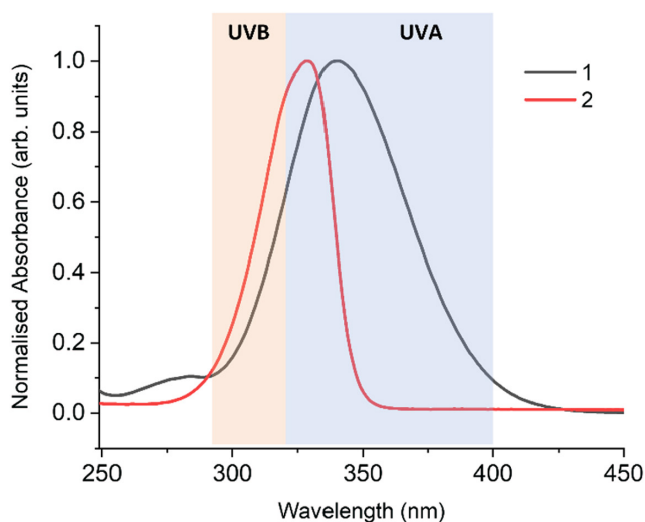

FIGURE 2 UV-visible spectra of **1** and **2** are displayed with the UVB (290–320 nm) and UVA (320–400 nm) regions highlighted. Absorption is normalized to the peak maximum (**1** $\lambda_{max} = 341$ nm and **2** $\lambda_{max} = 329$ nm).

The variable c_I is the initial concentration before irradiation and c_F is the concentration after irradiation. By the widely known Bouguer-Beer-Lambert law[51]; the concentration of the solute is directly proportional to absorption and so the change in the concentration can be measured by considering either the change in the absorbance at the peak maximum or the change in the area under the curve (AUC) across a selected region of the spectrum. An area under curve index (AUCI), which is a ratio of the final area (AUC$_F$) and the initial area (AUC$_I$) for the irradiation, can then be calculated by the following equation:

$$\text{AUCI} = \frac{\text{AUC}_F}{\text{AUC}_I}. \qquad (2)$$

The steady-state irradiation data obtained from the solar simulator are presented in Figure 3. Across 2 h of continuous irradiation, the profile of **2** did not change significantly (<1%), whereas irradiation of **1** was accompanied by a 12.3% decrease at the peak absorbance. The AUCI (320–400 nm) for **1** is calculated as 0.88 and the AUCI for **2** is >0.99. An AUCI >0.80 has previously been used as a criterion for a photostable molecule.[52,53] By this AUC method, both molecules can be considered photostable. These irradiation results will be returned later as a comparison to the TAS.

To investigate the femtosecond (10^{-15} s) to nanosecond (10^{-9} s) behavior of **1** and **2**, ultrafast TEAS measurements were performed, and the data are displayed in Figure 4. Firstly, attention is focused on a full analysis of the results for **1**; and then proceeding to **2** in the following section. A visual inspection of the TAS of **1** beginning at time zero shows a ground state bleach (GSB) feature that is centered at the blue edge of the spectrum (~340 nm). In a GSB, light that was previously absorbed in that spectral region by molecules in the ground state now passes through the sample and reaches the detector; thus, the feature is characterized by a negative absorption (i.e., $I > I_0$ where then $\Delta OD = \log_{10}(I_0/I) < 0$). There is also a broad stimulated emission (SE) feature which is immediately evident on the fs timescale after excitation and which spans the red edge of the spectrum (500–700 nm region); and is likewise detected by a negative ΔOD. Further, there is a broad excited state absorption (ESA) feature that appears across 380–550 nm and which lasts on the sub-ps to ps timescale, characterized by a positive absorption due to the opposite logic as the GSB and SE features (i.e., $I < I_0$). The ESA in the spectral region 375–450 nm is observed immediately following photoexcitation and the broadening out to 550 nm is shifted from time zero; possibly due to competing stimulated emission at early time which is stronger in intensity. Finally, after ~10 ps, the ESA has mostly decayed but there is a long-lived component that persists beyond
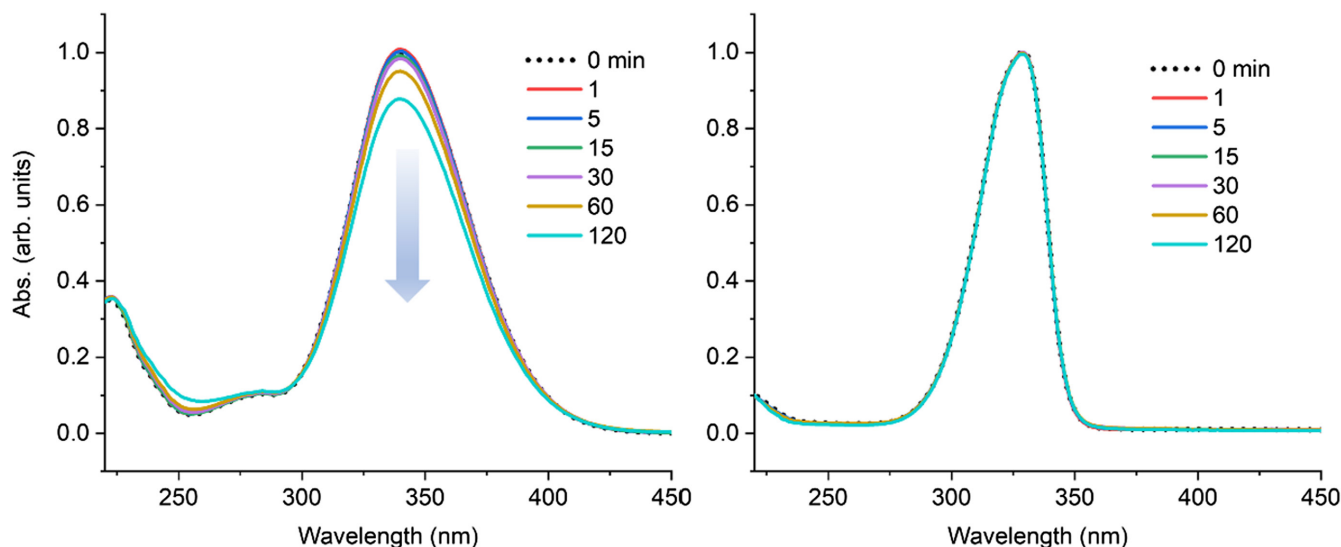
FIGURE 3 Photostability as measured by the change in UV-visible absorption of **1** (left) and **2** (right) in simulated solar conditions in ethanol across 2-h irradiation. Absorbance has been normalized to the peak maximum. A plot of the linear photodegradation of **1** is included in the Figure S4.

the time window of the experiment, appearing as a GSB at ~340 nm and an ESA at ~380 nm.

The photodynamic processes that produce spectral signals and their temporal evolution can be defined by time constants that are extracted from the data by our fitting procedure. As the TEAS appeared initially similar to that reported in previous literature, the following discussion and time constant assignments were guided by previous work.[32] The evolution-associated difference spectra (EADS) produced from this data fit are included along with the TEAS to support the final assignments (Figure 4).

The whole spectral region of the probe was used in a sequential model minus the 340–355 nm region, due to imperfect pump beam subtraction. In the case of **1**, the sequential kinetic fit extracted four-time constants (see Table 1). The process with a lifetime of ~150 fs (τ_{e1}) is attributed to a geometry rearrangement (involving both solvent and solute) as population evolves out of the Franck-Condon region of the initially prepared first electronically excited state (S_1), as evidenced by the decay of the SE. The large Stokes shift in the SE implies a large geometry change from the Franck-Condon geometry; we return to discuss this below considering the steady-state fluorescence spectra. This assignment is in accordance with the previous study by Losantos et al.[27] The second time constant, ~620 fs (τ_{e2}), is assigned to population of **1** as it progresses toward the S_1/S_0 conical intersection (CI) on the S_1 potential energy surface and then passes through the CI to populate a vibrationally hot electronic ground state. The third time constant of ~3 ps (τ_{e3}) is attributed to the slower process of vibrational cooling in the vibrationally hot ground state, via vibrational energy transfer with both

intramolecular and intermolecular components. A blue-shift, observed by a tailing off of the ESA in the TEAS ~380–400 nm is also indicative of ground-state vibrational cooling and this is reflected in the blueshift between the EADS of τ_{e2} and τ_{e3}. The final time constant is >3 ns (τ_{e4}) and this is assigned to a persistent long-lived feature that is present after ~10 ps with no spectral changes out to the final time delay of this experiment ($\Delta t = 3$ ns after photoexcitation).

A comparison of the absorbance spectra before and after 2 h of solar irradiation can be used to evaluate whether the feature at ~380 nm is due to the formation of a stable photoproduct (Figure S5). Given that the long-lived feature on the TEAS (>3 ns) is not present in the difference spectrum at longer times (2 h), this could indicate that a minor portion of population becomes trapped in an excited state but then resolves at longer times. Additionally, however, a photoisomer with a 30-nm redshift compared to the parent molecule identified in the calculations (see farther below) coincides with the observed ESA. A predicted low barrier in the thermal equilibrium between the parent molecule and the photoisomer would also likely allow the parent molecule to recover beyond 3 ns. Furthermore, as we did not observe any degradation when **1** was irradiated with monochromatic light for 1 h (Figure S6), which more closely mimics the TEAS experiment compared to the solar simulator experiment, it is believed that any photoisomer formed (or trapped excited state population) does eventually return to the ground state. Returning to the possibility of excited state population, it is proposed that population would mostly find its way to the S_1/S_0 CI beyond 3 ns as only weak fluorescence is observed (the
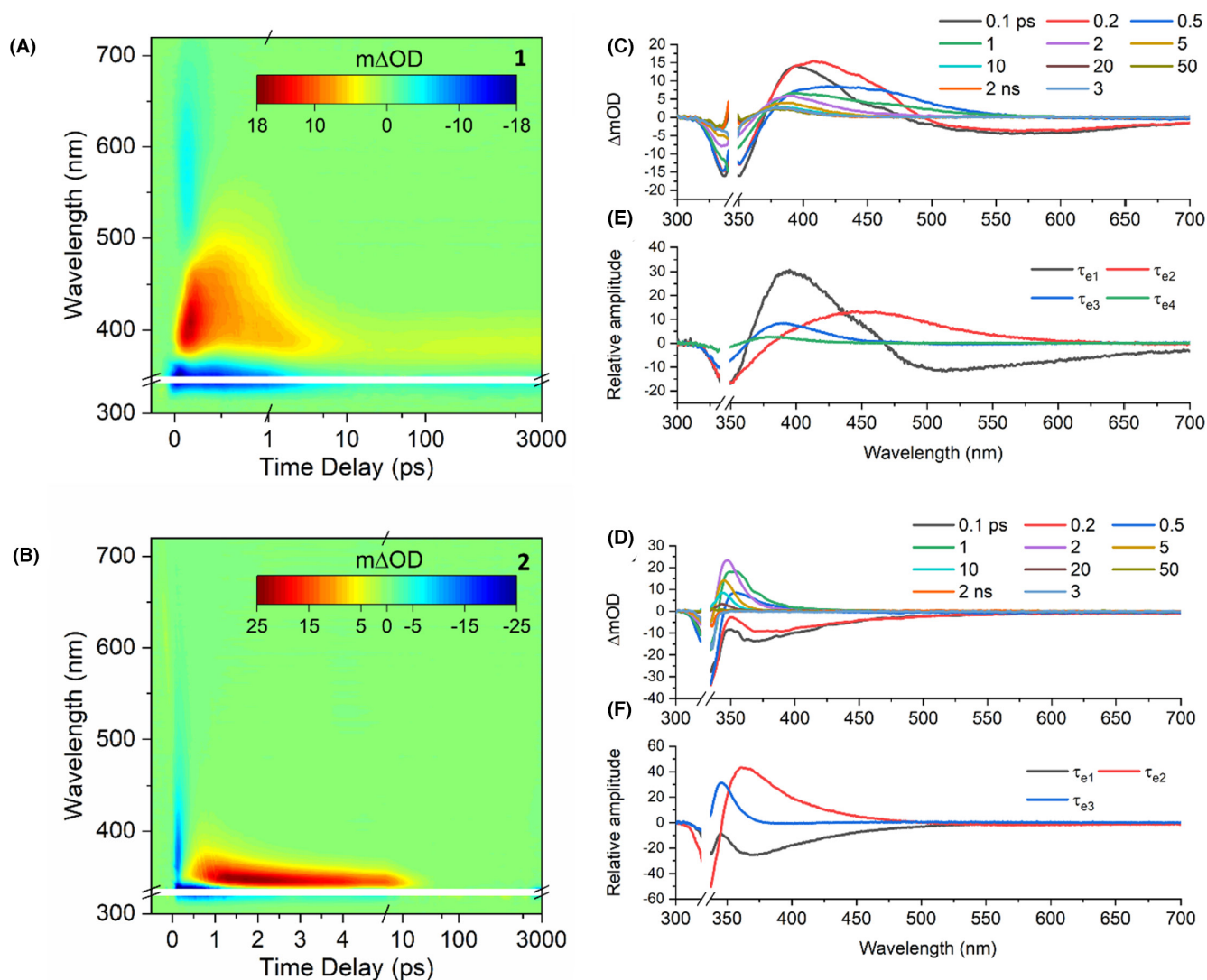
FIGURE 4 TAS of **1** (A) and **2** (B) presented as false-color heat maps. The time delay scale is linear to 1 ps and then logarithmic to 3000 ps in (A) while in (B) the scale is linear to 5 ps and logarithmic thereafter. The region between 340–349 and 320–334 nm has been omitted for all spectra for **1** and **2**, respectively, due to imperfect pump pulse subtraction. Selected time delays from the TAS are plotted as lineouts in **1** (C) and **2** (D) beside the corresponding TAS. The EADS of **1** (E) and **2** (F) produced by the fitting procedure.

quantum yield was determined to be <1%); implying that any trapped population only partially recovers via a radiative decay mechanism (Figure S7). The large Stokes shift in the fluorescence spectra can be explained by the large geometry change between the Franck-Condon geometry and the S_1 minimum geometry.[27] The similarity between the fluorescence spectra and the SE observed in the TAS suggests that excited state population that drives this emission is localized in a similar molecular geometry. We add that the SE signal may be artificially shifted due to the competing ESA at shorter wavelengths. Finally, while it is not truly resolved whether trapped population or the presence of a photoisomer is at play, it is worth noting that a loss of the absorbance over 2 h of solar-simulated irradiation study does indicate that the parent molecule **1**

could be sensitive to some photodegradation in a real-life environment.

Transient vibrational absorption spectroscopy data were obtained for additional insight into the putative photoprotective mechanism, specifically into the nature of the vibrational relaxation in the S_0 and to complement time constant assignment for the TEAS data. To cover the regions at 1480–1660 cm^{-1}, the probe beam was centered at two different wavenumber regions and the data were stitched together by matching to the signal intensity at 1535 cm^{-1}. The resulting spectra (Figure 5A) contain three negative features; namely, a sharp and intense feature at ~1510 cm^{-1}, a broad and weaker feature at ~1535 cm^{-1}, and a third weak feature at ~1610 cm^{-1}. These features correspond to the GSB of

TABLE 1 The time constants listed in the table for TEAS were obtained through a global fit of the data with a sequential model and are quoted with associated errors which are half the instrument response estimated using solvent-only TAS (Figure S8); the quality of the fit can be assessed through the fitting residuals (Figure S9).

	Time constant (Molecule 1)	Time constant (Molecule 2)	Process
TEAS			
τ_{e1} (fs)	150 ± 60	470 ± 60	FC
τ_{e2} (fs)	620 ± 60	450 ± 60	CI
τ_{e3} (ps)	2.99 ± 0.06	5.74 ± 0.06	VC
τ_{e4} (ns)	>3		PP
TVAS			
τ_{v1} (ps)	$4.2 \,(\pm 0.3)$	$2.4 \,(\pm 0.5)$	VC
τ_{v2} (ps)	>1000	$11.1 \,(\pm 7.6)$	VC

Note: The time constants listed in the table for TVAS were obtained through a bi-exponential fit of a chosen integrated region and the quoted errors are those output by the fit. The final time constant for **1** is beyond the experimental time window of the TEAS experiment (3 ns).

Abbreviations: CI, conical intersection; FC, evolution out of the Franck-Condon region; PP, trapped or long-lived population/photoproduct; TAS, transient absorption spectra; TEAS, transient electronic absorption spectroscopy; TVAS, transient vibrational absorption spectroscopy; VC, vibrational cooling.

1's S_0 vibrational modes in this region as evidenced by their spectral match with the FTIR spectrum (overlaid dashed spectrum). A bi-exponential decay was chosen to fit the most prominent feature (by integrating across $1504–1524 \, cm^{-1}$), modeling the GSB recovery in the first 1 ns after photoexcitation (Figure 5B). The other features are presented for comparison in the Supporting Information (Figure S10). The first time constant of the main feature fit, 4.2 ps (τ_{v1}), is attributed to vibrational cooling and is on the same timescale as the component of vibrational cooling seen on the TEAS (~3 ps), which supports our assignment. The second time constant, >1 ns (τ_{v2}), extends beyond the experiment time window and describes incomplete GSB recovery; indeed, there is only ~83% recovery overall within 1 ns for this feature. This is in accordance with the TEAS measurements as there was the presence of a remnant GSB beyond 3 ns. The remaining ~17% that has not recovered is believed to be due to photoisomer formation and perhaps trapped population in the excited state as described above.

Now focus turns to an analysis of **2**, beginning with the TEAS. Similar to **1**, there is a GSB feature from time zero centered at the blue edge of the spectrum (~340 nm). There is also a broad stimulated emission SE feature which is immediately evident on the fs time scale after excitation and spans the red edge of the spectrum (500–700 nm region). There is an ESA that appears across 340–370 nm and

which lasts on the sub-ps to ps scale and a slight shift from time zero may indicate that the absorption is the result of a relaxation process.

The whole spectral region of the probe was used for the fit of **2** minus the 320–334 nm region due to imperfect pump subtraction. The sequential kinetic fit extracted only three time constants (see Table 1). The process with a lifetime of ~470 fs (τ_{e1}) is the first extracted time constant and is assigned to geometry and solvent rearrangement as population evolves out of the Franck-Condon region of the initially prepared first electronically excited state (S_1) and along the S_1 coordinate as evidenced by the decay of the stimulated emission. The second time constant, ~450 fs (τ_{e2}), is assigned to the population of **2** as it progresses toward the S_1/S_0 CI on the electronic excited state potential energy surface and then passes through the CI to populate the vibrationally hot electronic ground state. Low levels of SE at the red edge of the probe window in the EADS for τ_{e2} (Figure 4F) support this assignment. The third time constant of ~5.7 ps (τ_{e3}) is attributed to the slower process of vibrational cooling from the vibrationally hot ground state, via vibrational energy transfer, both intramolecular and intermolecular. A blueshift of the ESA in the TAS in this region is also indicative of ground-state spectrum cooling. A negative artifact that appears at longer times (~3 ns) was investigated in a separate photoproduct scan and was found not to be a significant feature (Figure S11).

Transient vibrational absorption spectroscopy data were also acquired for **2** using a single probe to cover the regions $1480–1660 \, cm^{-1}$. The obtained spectra (Figure 5C) have a prominent feature at $~1550 \, cm^{-1}$. A bi-exponential decay fit was used across the feature ($1540–1560 \, cm^{-1}$) to model the recovery in the first 1 ns (Figure 5D). The first time constant of this fit, 2.4 ps (τ_{v1}), is attributed to vibrational cooling of the S_0. The second constant, ~11 ps (τ_{v2}) with a large associated error (reflected in the scattered data points around the fit), was found to be a minor contributor that could indicate a slower component of vibrational cooling in the electronic ground state, for example, $\nu_0 \leftarrow \nu_1$ or remnant population that funnels through the S_1/S_0 CI at a slower rate. The time constant attributed to vibrational cooling in the TEAS is an intermediate value of the two time constants extracted from the TVAS, suggesting that of the two methods, only TVAS was able to resolve the vibrational cooling into two parts. Although there is evidence that the ESA extends out to >10 ps in the TEAS (Figure S12), our fitting model was unable to extract a longer lifetime; perhaps due to a drop-off in the signal. In accordance with the TEAS results, 100% GSB recovery of **2** was observed. Weak fluorescence was also observed in **2** when irradiated at the peak maximum (Figure S7); the quantum yield was determined to be ~1%.

To compare the two molecules directly, the relaxation dynamics in both have sub-ps excited state lifetimes
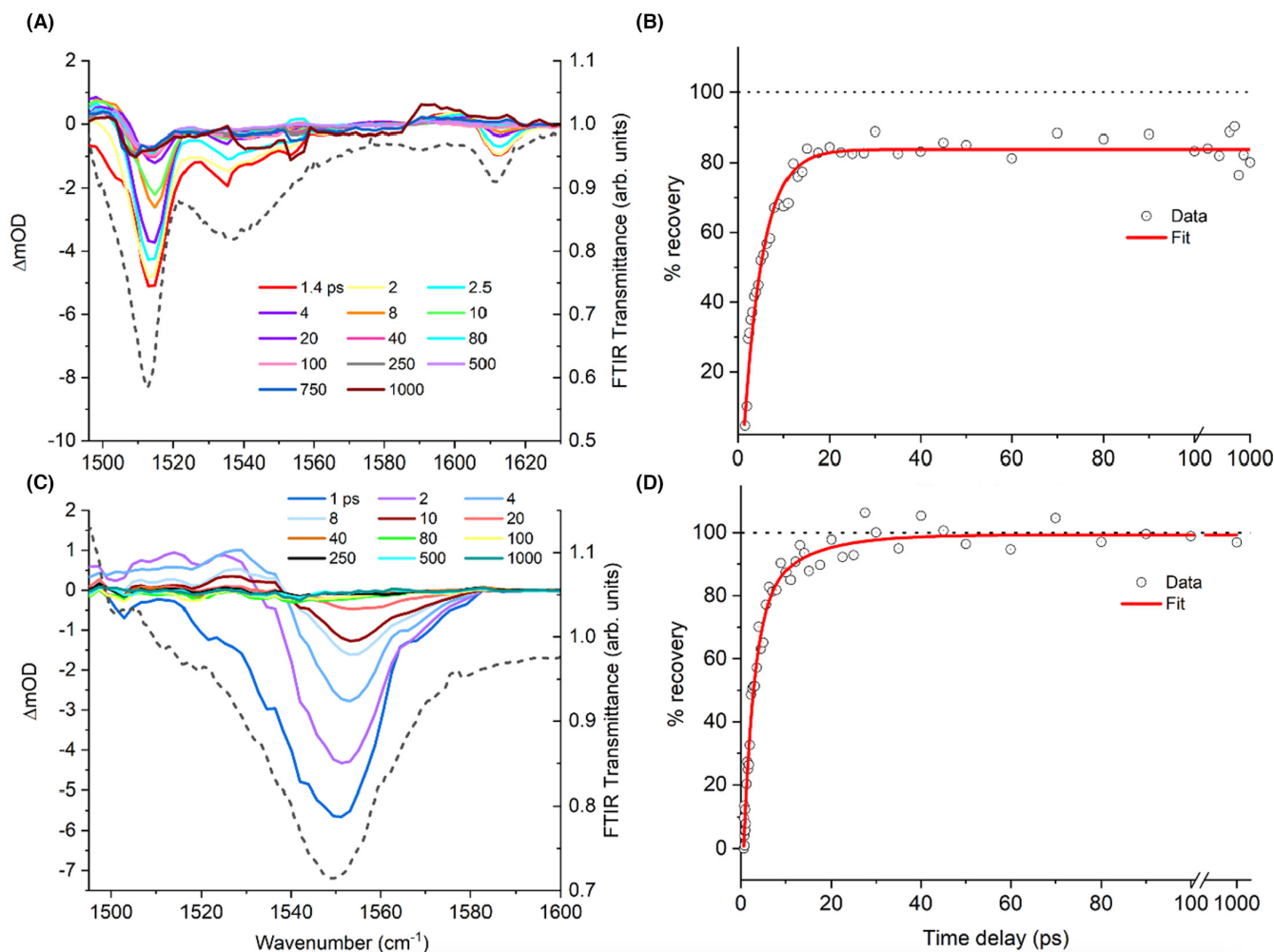
FIGURE 5 (A) Transient vibrational absorption spectra (smoothed) of **1**. The most negative trace (black, dashed line) is the smoothed FTIR spectrum with the transmittance scale provided on the right side of the plot. (B) Bi-exponential fit of the percentage recovery of the GSB feature in **1**. The integration region for the fit was 1504–1524 cm^{-1} and the two extracted time constants are $\tau_{v1} = 4.2$ (± 0.3) ps and $\tau_{v2} = >1$ ns. The scale is linear up to 100 ps and logarithmic after, up to 1 ns. (C) Transient vibrational absorption spectra (smoothed) of **2**. The most negative trace (black, dotted) is the smoothed FTIR spectrum with the transmittance scale provided on the right side of the plot; (D) Bi-exponential fit of the percentage recovery of **2**. The integration region for the GSB feature fit is 1540–1560 cm^{-1} and the two extracted time constants are $\tau_{v1} = 2.4$ (± 0.5) ps and $\tau_{v2} = 11.1$ (± 7.6) ps. The scale is linear up to 100 ps and logarithmic after, up to 1 ns.

followed by a few picoseconds of cooling; suggesting quick and efficient relaxation pathways exist in both. However, molecule **1** seems to degrade more than **2** as observed in the solar simulator study. The persistent GSB in both the TEAS and TVAS studies of **1** could be linked to this degradation. The ~17% unrecovered ground-state population for **1**, despite recovering at longer timescales based on no observed degradation in the monochromatic irradiation experiment (cf. Figure S6), may have repercussions in a more complex environment, such as in a sunscreen formulation in the real world where excited molecules could be more reactive with other molecules and reduce the effective UV protection, etc. Further, on irradiating both samples in a closer-to-real-life irradiation environment

with a solar simulator, **2** proved to be the more stable of the two molecules in this study.

Computational results discussion

To complement the time-resolved experiments, a series of on-the-fly non-adiabatic molecular dynamics calculations were performed to determine comprehensively how these molecules evolve after absorption of light. Previous results on related compounds produced unexpected evidence for different deactivation pathways based on static calculations.[27] As discussed above, an alternative relaxation mechanism for MAA analogs dependent on the chemical

structure of the ring substituents may involve a conical intersection (CI) comprising C=N double bond isomerization in contrast to the conventional ring buckling deactivation channel found in natural MAAs.[26–28] Extended orbital conjugation with the aromatic ring in the C=N-Ph moiety, as in **1**, is thus suggestive of an alternative deactivation channel of lower energy compared to the ring buckling CI geometry. Further, a minimum in the excited state potential energy surface was found in the aforementioned computational studies, which could be responsible for any longer lived excited state species, contributing to the ESA signal and persistent GSB. Even if the computed static barrier to the CI was low, the presence of this barrier could significantly influence the dynamics of molecule **1** with respect to **2**. Complementary to the experimental data, we sought to rationalize the coincidence of the two mechanisms. Such a model that includes the possibility of accessing both mechanisms could give us a handle to control selectively the photoprotection mechanism by deliberately selecting the substituents on the same core system in future studies.

With this motivation in mind, we focused on a high-level approach with a moderate sampling (50 trajectories) and a reduced timescale (extending to 800 fs) with a focus on relaxation to the ground state; therefore, the use of multireference methods like CASSCF is mandatory (see Supporting Information for active space orbitals, Figures S13 and S14). Due to this high-demand methodology, the computational cost of the simulations required to describe relaxation of the system up to, for instance, 1.5 ps would be prohibitively high and justifies our choice to compromise. The ensemble of trajectories was analyzed using a series of homemade scripts to extract the main parameters, such as spatial and population information.

As mirrored by the experimental results, the long-lived components identified in **1** but not for **2** suggest that some population of **1** does not return to its original state geometry, which also agrees with the incomplete GSB recovery observed experimentally and the previously described minimum in the excited state identified by static calculations. To evaluate the excited state decay, we computed and averaged the population after excitation to S_1 through the ensemble of trajectories (see Figure 6A). Firstly, we note an incomplete average recovery of the ground state during the computed time as both compounds have a remaining population of ca. 0.2 (20%)—and so in this case, no obvious difference between **1** and **2** can be drawn from this feature. In contrast, in terms of the timescale of the deactivation process, the excited state population of **2** decreases moderately faster than that of **1**. An approximate value for the half-life can be estimated by the time at which the population reached 0.5 (i.e., 50%) here, around 530 and 420 fs, for **1** and **2**, respectively. The data obtained are in qualitative agreement with the experimental sub-ps excited state lifetimes for both molecules as it must be considered that in the experiment a convolution of additional factors are at play, and thus direct comparison is not advised. Also, the simulations were carried out in vacuum, negating relevant sunscreen-solvent interactions which can play a significant role in these processes.

Likewise, the analysis of the trajectories allows a deeper understanding of the surface hopping time evolution for the different trajectories. It should be noted that Tully's fewest switch surface hopping algorithm was used to compute the hopping probability and so the total number of switches can vary. This algorithm allows the system to jump more than once between the different electronic surfaces, it being not compulsory to have 50 (for the 50 trajectories) or even the same number of hopping points in both systems. The evolution of the hopping times for each compound is presented in Figure 7.
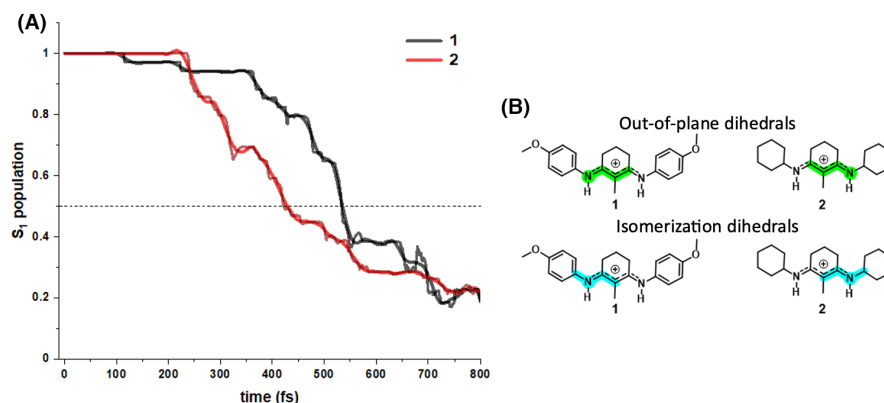
FIGURE 6 (A) Average evolution of S_1 population through the ensemble of trajectories. A smoothed plot is presented in bold; while the thin line encodes the original data. (B) Representative dihedral angles were analyzed along the trajectories. It should be noted that in each system, the symmetrically equivalent dihedral was analyzed as well as the highlighted angle to account for the loss of symmetry in the molecule as it evolves along the trajectories.
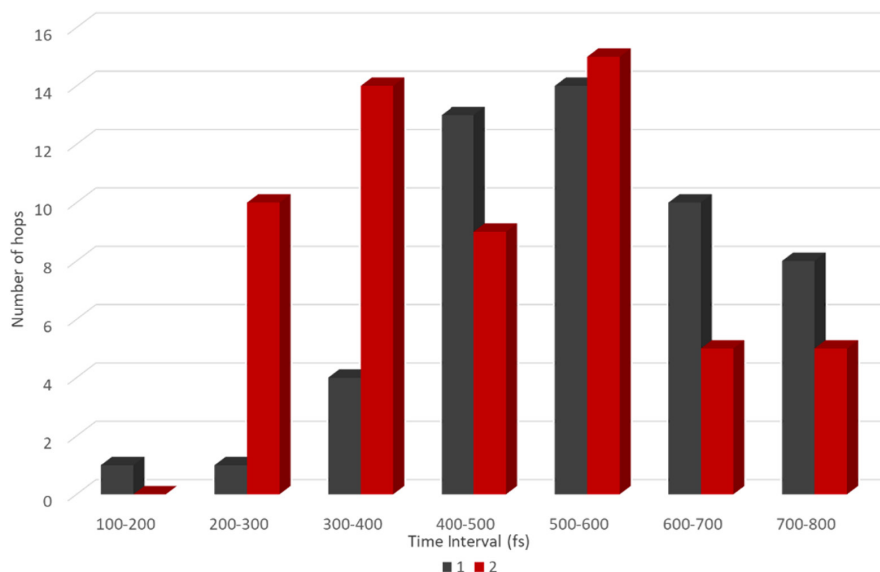
FIGURE 7   Histogram containing the accumulated time of hopping points for **1** (black) and **2** (red).

The observed trend in the histogram agrees with the population analysis and confirms a slightly faster deactivation for **2** compared to **1**; even if the former compound demonstrates a larger dispersion in hopping times. This is in qualitative agreement with the experimental results that show that both **1** and **2** relax on a sub-picosecond timescale. It should be noted that only trends can be discussed when comparing these two different approaches.

Furthermore, and perhaps more interestingly, a detailed analysis of the obtained trajectories can be used to draw mechanistic conclusions. As previously stated, two main deactivation mechanisms are proposed to be available for **1** and **2**, namely, the well-documented ring buckling deformation and the *new* C=N isomerization pathway. Both pathways involve some geometrical deformations which can be monitored through the changes in the dihedral angles highlighted in Figure 6B above. The prevalence of either of these mechanisms can be explored by monitoring the geometrical deformations that lead to relaxation to the ground state. Due to the initial symmetry of the molecules, the dihedral angle to be considered implies both sides of the molecule, meaning that four dihedrals should be examined for each system.

The evolution with time of the four dihedrals for all the computed trajectories is represented in Figure 8. For clarity, the two out-of-plane (i.e., ring buckling) and the two isomerization dihedrals are plotted together for each compound.

In our results, a clear difference was found between compounds **1** and **2**, depicting completely different behavior after light absorption. In the case of compound **2**, ring buckling is the only deactivation pathway observed and it is only coupled to minor modifications in the dihedral

angles of the cyclohexyl rings. This is clearly shown by the large changes in the out-of-plane dihedral angles (top right of Figure 8) and the relatively small deformations in the C=N-Ph moiety (bottom right of Figure 8). On the other hand, compound **1** mainly follows the C=N isomerization pathway, as represented by the significant modification in the corresponding angles (bottom left of Figure 8). It is worth noting that each molecule follows exclusively one deactivation mechanism (as no trajectory following the alternative mechanisms was found simultaneously). However, both mechanisms are, thus, in their own right responsible for the experimentally observed photostability of these compounds. This divergent behavior between **1** and **2** is in agreement with the previous study suggesting a change in the deactivation pathways can be affected by modifying the chemical structure of this type of compound.[26] For MAA analogs such as **1** and **2**, on top of the change in the photoprotection mechanism, substitution with aromatic moieties implies an increase in the conjugation and consequently a moderate redshift in the absorption profile.

To better illustrate the geometric deformations involved in both systems, representative geometries in the hopping region are presented in Figure 9. The hopping geometries found for different trajectories for each compound are similar and are not shown. Those are very close to the conical intersection geometries already computed for these molecules through the previously mentioned static calculations. The relevant geometrical deformations can be clearly seen in these hopping geometries. For **1**, the C=N isomerization is evident by the ca. 90° twist (highlighted in Figure by an orange arrow) in one of the imine moieties while the six-membered rings remain mainly
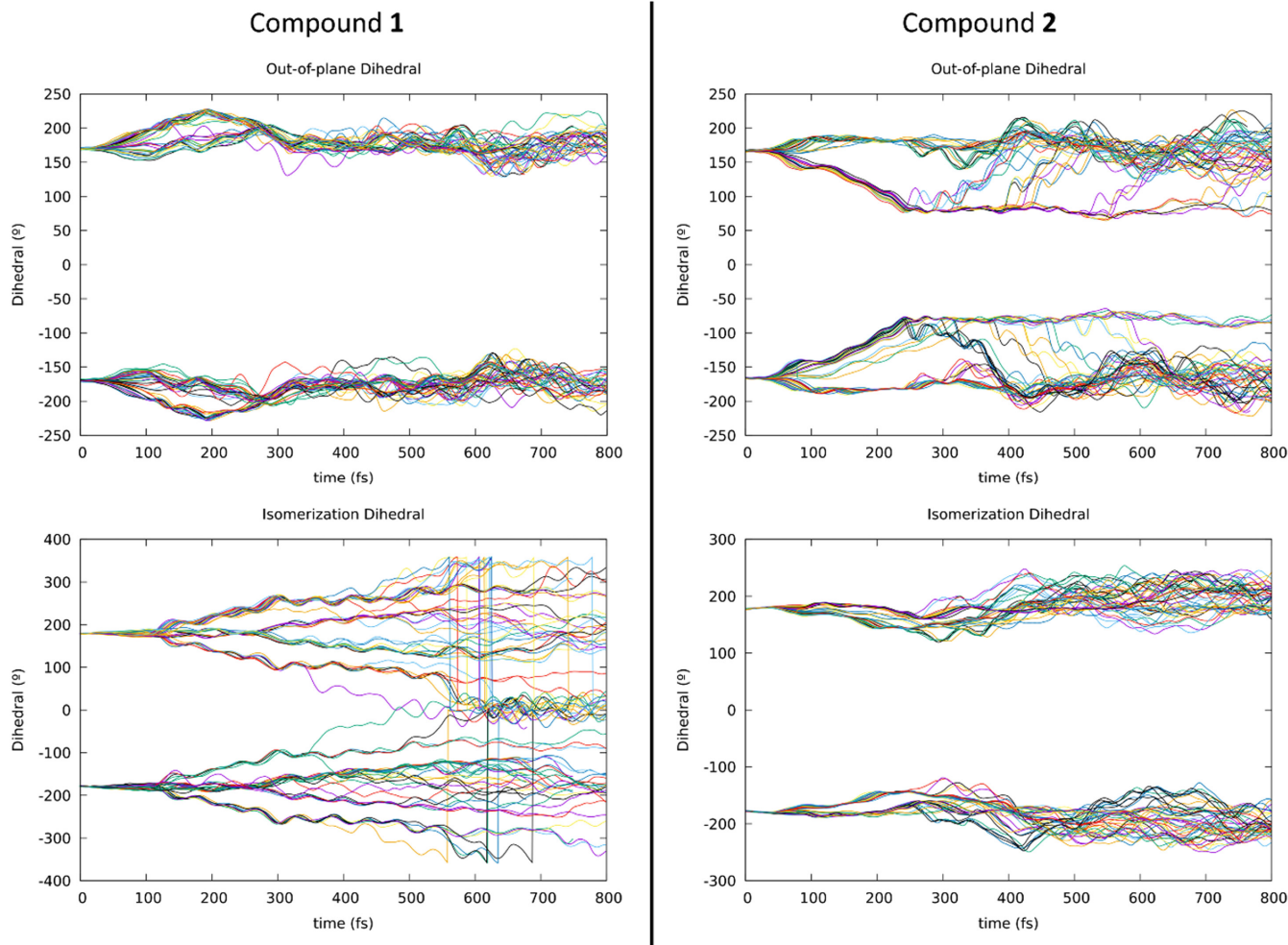
FIGURE 8 Geometrical evolution with time monitored by dihedral angle analysis. It should be noted that the numerical gap observed in the isomerization dihedral (compound **2**, bottom panel) is due to a mathematical transformation to avoid values greater than 360°, which are modified to 0°.

planar. In contrast, **2** does not change the initial planar conformation in both C=N bonds, the cycle distorts and one of the imine substituents moves out of the plane of the ring (highlighted in Figure 9).

These geometric changes with their associated potential energy landscapes can explain the differences in the photoprotection mechanism. From the results in Figure 8, it is evident that photoisomerization along the C=N bond is the main deactivation pathway in **1**. This implies the formation of a photoisomer in the ground state following excited state deactivation (see Figure 10) which can be linked to the fourth time constant, τ_4, which extends beyond the final time delay of the experimental window, >3 ns. The formation of the photoisomer is also suggested by the NAMD simulations, as a significant part of the ensemble remains in a Z conformation, ca. 0°. In an attempt to better understand the behavior of the formed photoisomer, we computed the relevant geometries at the PCM-MP2/6-31G* level of theory using ethanol as solvent to explore

the back conversion barrier and absorption spectra of the starting material and the photoisomer. As 13.8 kcal/mol is a relatively low barrier, rapid thermal back conversion would occur in accordance with the experimental results.

The key difference between **1** and **2** is the absence of chemical reactivity in the case of **2**, and this could have some practical implications for the use of these compounds as sunscreens and thus protectors of our DNA. For compound **2**, after light absorption, the excess energy is dissipated through a geometrical distortion that eventually leads to a vibrationally hot molecule in the ground state, without any predicted or observed net reactivity. In contrast, for **1** the deactivation implies a photochemical reaction that yields a photoisomer, albeit with recovery at longer times. Certainly, the optical properties of the photoisomer are quite similar to the parent molecule, and both absorption bands overlap. In addition, the photochemical reaction that takes place could have an influence on the poorer photostability
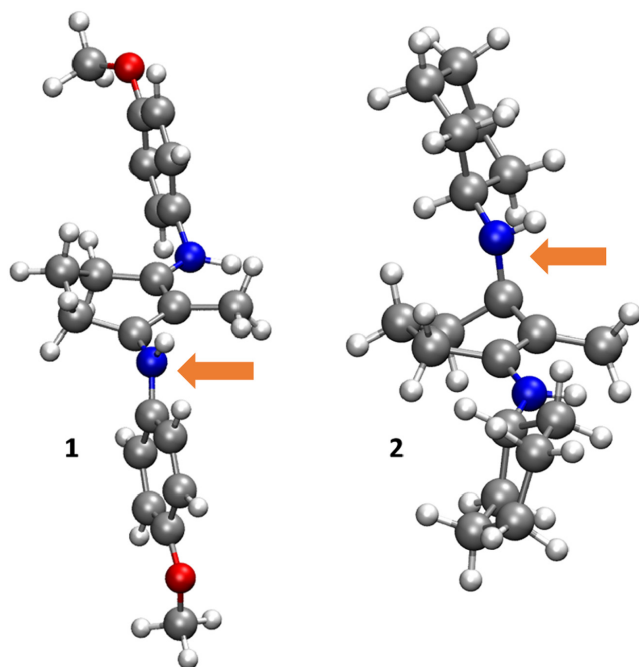
FIGURE 9 Representative hopping geometries of a representative trajectory for compounds **1** and **2**. Features discussed in the text are highlighted.
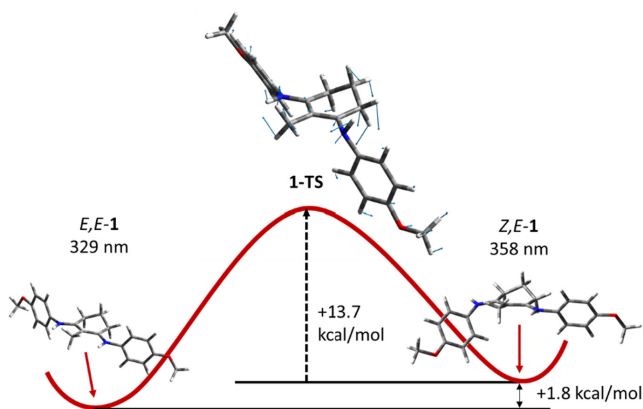
FIGURE 10 Schematic maximum absorbance and isomerization path of **1** and related TS with displacement vectors (Energies in kcal/mol referred to *E,E*-**1** and absorbance maxima in nm).

measured for this latter compound. Structural modifications introduced to affect the optical properties shown here also have a perceptible impact on the photoprotection mechanism and stability. These results clearly demonstrate the presence of competitive mechanisms involving photoisomerization and ring buckling even in otherwise similar molecules. This should be carefully considered in the design of the next generation of sunscreens based on the MAA core.

CONCLUSIONS

In this study, we utilized complementary experimental and computational techniques, in particular TEAS and TVAS, to understand photoprotection in two nature-inspired molecules in terms of their excited electronic and vibrational properties. These techniques work hand-in-hand since TVAS provides additional information about the GSB recovery that cannot be derived from TEAS alone. Supporting techniques (FTIR, long-term irradiation with UV-visible absorbance monitoring and fluorescence) link the ultrafast behavior to long-term activity, and thus provide a more complete picture of the longer term fate of each molecule in their role as a UV filter to protect DNA.

There is now sufficient experimental and computational evidence to suggest that, despite superficial similarities in their molecular structures, distinct mechanisms underlie the photodynamic behavior of related molecules **1** and **2**. Indeed, molecule **2** was designed specifically to permit further exploration of the dependence of the photodynamics on the identity of the N-substituents of the MAA-like molecular scaffold. Based on the experiment and CASSCF/NAMD calculations, **1** is suggested to follow a new, C=N isomerization pathway, not observed as yet in natural MAAs; while, from experiment and CASSCF results, **2** is suggested to follow a ring buckling mechanism much like the natural product MAAs. While both molecules demonstrate ultrafast dynamics, only **2** can be said to recover fully within the ps timescale after photoexcitation and to remain stable over longer timescales up to 2 h. In **1**, the presence of longer lived features recommends against prioritizing this molecule as a sunscreen active; however, we can suggest that **2** is probably the better synthetic analog and a potential new sunscreen active. More generally, this study represents how rational design can be used to adapt nature's preferred sunscreens for our own purposes; and also suggests that nature has already optimized this photoprotection mechanism.

Future work in line with this research could include skin models, toxicology studies and combining **2** with other sunscreening molecules in a formulation to increase the critical wavelength to meet industry requirements and robust protection for nucleic acids, including DNA can be guaranteed for the future. Future synthetic investigations could modify the pertinent substituent groups to investigate different alkyl moieties that may have minor effects without changing the operative IC mechanism. Molecules with a range of electron-withdrawing or electron-donating substituents could be proposed to probe the effect on the photodynamics, if any, of modifying the electronic properties of the system. Furthermore, a range of substituents with properties on the spectrum between those of **1** and **2** could be investigated to see if the mechanisms proposed could ever be truly coincident in one molecule.

ORCID

Adam M. Cowden ⓘ https://orcid.org/0000-0003-2695-6345
Raúl Losantos ⓘ https://orcid.org/0000-0001-5207-654X
Beatriz Peñín ⓘ https://orcid.org/0000-0003-4924-2628
Diego Sampedro ⓘ https://orcid.org/0000-0003-2772-6453
Vasilios G. Stavros ⓘ https://orcid.org/0000-0002-6828-958X

REFERENCES

1. Battie C, Jitsukawa S, Bernerd F, Del Bino S, Marionnet C, Verschoore M. New insights in Photoaging, UVA induced damage and skin types. *Exp Dermatol.* 2014;23:7-12. doi:10.1111/exd.12388

2. Brenner M, Hearing VJ. The protective role of melanin against UV damage in human skin†. *Photochem Photobiol.* 2008;84(3):539-549. doi:10.1111/j.1751-1097.2007.00226.x

3. Diffey BL. Sources and measurement of ultraviolet radiation. *Methods.* 2002;28(1):4-13. doi:10.1016/S1046-2023(02)00204-9

4. Fourtanier A, Moyal D, Seite S. UVA filters in sun-protection products: regulatory and biological aspects. *Photochem Photobiol Sci.* 2012;11(1):81-89. doi:10.1039/C1PP05152K

5. Robert M. Harmful effects of UVA on the structure and barrier function of engineered human cutaneous tissues. *Int J Radiat Biol.* 1999;75(3):317-326. doi:10.1080/095530099140492

6. Afonso S, Horita K, Sousa E Silva JP, et al. Photodegradation of Avobenzone: stabilization effect of antioxidants. *J Photochem Photobiol B.* 2014;140:36-40. doi:10.1016/j.jphotobiol.2014.07.004

7. Mturi GJ, Martincigh BS. Photostability of the Sunscreening agent 4-Tert-Butyl-4′-Methoxydibenzoylmethane (Avobenzone) in solvents of different polarity and Proticity. *J Photochem Photobiol Chem.* 2008;200(2–3):410-420. doi:10.1016/j.jphotochem.2008.09.007

8. Cosmetic Products Regulation, Annex VI – Allowed UV Filters; Regulation 1223/2009/EC on Cosmetic Products, as corrected by Corrigendum to Commission Regulation (EU) 2021/850, 17 June 2021; European Chemicals Agency. 2021. Accessed 07 February, 2022. https://echa.europa.eu/cosmetics-uv-filters

9. Serpone N. Sunscreens and their usefulness: have we made any progress in the last two decades? *Photochem Photobiol Sci.* 2021;20(2):189-244. doi:10.1007/s43630-021-00013-1

10. Narla S, Lim HW. Sunscreen: FDA regulation, and environmental and health impact. *Photochem Photobiol Sci.* 2020;19(1):66-70. doi:10.1039/C9PP00366E

11. Abiola TT, Whittock AL, Stavros VG. Unravelling the photoprotective mechanisms of nature-inspired ultraviolet filters using ultrafast spectroscopy. *Molecules.* 2020;25(17):3945. doi:10.3390/molecules25173945

12. Bandaranayake WM, Bemis JE, Bourne DJ. Ultraviolet absorbing pigments from the marine sponge *Dysidea herbacea*: isolation and structure of a new mycosporine. *Comp Biochem Physiol C Pharmacol Toxicol Endocrinol.* 1996;115(3):281-286. doi:10.1016/S0742-8413(96)00135-1

13. Cockell CS. The ultraviolet history of the terrestrial planets — implications for biological evolution. *Planet Space Sci.* 2000;48(2–3):203-214. doi:10.1016/S0032-0633(99)00087-2

14. Cockell CS. Ultraviolet radiation and the photobiology of earth's early oceans. *Orig Life Evol Biosph.* 2000;30(5):467-500. doi:10.1023/A:1006765405786

15. Shick JM, Dunlap WC. Mycosporine-like amino acids and related Gadusols: biosynthesis, accumulation, and UV-protective functions in aquatic organisms. *Annu Rev Physiol.* 2002;64(1):223-262. doi:10.1146/annurev.physiol.64.081501.155802

16. Whittock AL, Auckloo N, Cowden AM, et al. Exploring the blueprint of photoprotection in mycosporine-like amino acids. *J Phys Chem Lett.* 2021;12(14):3641-3646. doi:10.1021/acs.jpclett.1c00728

17. Balskus EP, Walsh CT. The genetic and molecular basis for sunscreen biosynthesis in cyanobacteria. *Science.* 2010;329(5999):1653-1656. doi:10.1126/science.1193637

18. Llewellyn CA, Airs RL. Distribution and abundance of MAAs in 33 species of microalgae across 13 classes. *Mar Drugs.* 2010;8(4):1273-1291. doi:10.3390/md8041273

19. Rastogi RP, Sonani RR, Madamwar D. UV photoprotectants from algae—synthesis and bio-functionalities. *Algal Green Chemistry.* Elsevier; 2017:17-38.

20. Rosic NN. Recent advances in the discovery of novel marine natural products and mycosporine-like amino acid UV-absorbing compounds. *Appl Microbiol Biotechnol.* 2021;105(19):7053-7067. doi:10.1007/s00253-021-11467-9

21. Shaath NA. Ultraviolet filters. *Photochem Photobiol Sci.* 2010;9(4):464-469. doi:10.1039/b9pp00174c

22. Geraldes V, Pinto E. Mycosporine-like amino acids (MAAs): biology, chemistry and identification features. *Pharmaceuticals.* 2021;14(1):63. doi:10.3390/ph14010063

23. Bens G. Sunscreens. In: Reichrath J, Back N, Cohen IR, Lajtha A, Lambris JD, Paoletti R, eds. *Sunlight, Vitamin D and Skin Cancer.* Vol 624. Springer New York; 2008:137-161.

24. Conde FR, Churio MS, Previtali CM. Experimental study of the excited-state properties and photostability of the mycosporine-like amino acid palythine in aqueous solution. *Photochem Photobiol Sci.* 2007;6(6):669-674. doi:10.1039/b618314j

25. Osterwalder U, Herzog B. The long way towards the ideal sunscreen—where we stand and what still needs to Be done. *Photochem Photobiol Sci*. 2010;9(4):470-481. doi:10.1039/b9pp00178f

26. Losantos R, Funes-Ardoiz I, Aguilera J, et al. Rational design and synthesis of efficient sunscreens to boost the solar protection factor. *Angew Chem Int Ed Engl*. 2017;56(10):2632-2635. doi:10.1002/anie.201611627

27. Losantos R, Lamas I, Montero R, Longarte A, Sampedro D. Photophysical characterization of new and efficient synthetic sunscreens. *Phys Chem Chem Phys*. 2019;21(21):11376-11384. doi:10.1039/C9CP01267B

28. Sampedro D. Computational exploration of natural sunscreens. *Phys Chem Chem Phys*. 2011;13(13):5584-5586. doi:10.1039/c0cp02901g

29. Hatakeyama M, Koizumi K, Boero M, et al. Unique structural relaxations and molecular conformations of Porphyra-334 at the excited state. *J Phys Chem B*. 2019;123(36):7649-7656. doi:10.1021/acs.jpcb.9b03744

30. Arbeloa EM, Bertolotti SG, Churio MS. Photophysics and reductive quenching reactivity of Gadusol in solution. *Photochem Photobiol Sci*. 2011;10(1):133-142. doi:10.1039/C0PP00250J

31. Hatakeyama M, Nakamura S. Intrinsic nature of the ultrafast deexcitation pathway of mycosporine-like amino acid porphyra-334. *J Phys Chem A*. 2022;126(41):7460-7467. doi:10.1021/acs.jpca.2c05034

32. Woolley JM, Staniforth M, Horbury MD, Richings GW, Wills M, Stavros VG. Unravelling the photoprotection properties of mycosporine amino acid motifs. *J Phys Chem Lett*. 2018;9(11):3043-3048. doi:10.1021/acs.jpclett.8b00921

33. Whittock AL, Woolley JM, Auckloo N, Corre C, Stavros VG. Investigating the ultrafast dynamics and long-term photostability of an isomer pair, usujirene and palythene, from the mycosporine-like amino acid family. *Molecules*. 2022;27(7):2272. doi:10.3390/molecules27072272

34. Ni G, Li G, Boriskina SV, et al. Steam generation under one sun enabled by a floating structure with thermal concentration. *Nat Energy*. 2016;1(9):16126. doi:10.1038/nenergy.2016.126

35. Grubb MP, Orr-Ewing AJ, Ashfold MNR. KOALA: a program for the processing and decomposition of transient spectra. *Rev Sci Instrum*. 2014;85(6):064104. doi:10.1063/1.4884516

36. Mullen KM, Van Stokkum IHM. TIMP: an *R* package for modeling multi-way spectroscopic measurements. *J Stat Softw*. 2007;18(3):1-46. doi:10.18637/jss.v018.i03

37. Snellenburg JJ, Laptenok SP, Seger R, Mullen KM, Van Stokkum IHM. Glotaran: a *Java*-based graphical user Interface for the *R* package TIMP. *J Stat Softw*. 2012;49(3):1-22. doi:10.18637/jss.v049.i03

38. Whittock AL, Turner MAP, Coxon DJL, Woolley JM, Horbury MD, Stavros VG. Reinvestigating the photoprotection properties of a mycosporine amino acid motif. *Front Chem*. 2020;8:574038. doi:10.3389/fchem.2020.574038

39. Roos BO, Taylor PR, Sigbahn PEM. A complete active space SCF method (CASSCF) using a density matrix formulated super-CI approach. *Chem Phys*. 1980;48(2):157-173. doi:10.1016/0301-0104(80)80045-0

40. Tully JC. Molecular dynamics with electronic transitions. *J Chem Phys*. 1990;93(2):1061-1071. doi:10.1063/1.459170

41. Hammes-Schiffer S, Tully JC. Proton transfer in solution: molecular dynamics with quantum transitions. *J Chem Phys*. 1994;101(6):4657-4667. doi:10.1063/1.467455

42. Fdez Galván I, Vacher M, Alavi A, et al. OpenMolcas: from source code to insight. *J Chem Theory Comput*. 2019;15(11):5925-5964. doi:10.1021/acs.jctc.9b00532

43. Aquilante F, Autschbach J, Baiardi A, et al. Modern quantum chemistry with [open]Molcas. *J Chem Phys*. 2020;152(21):214117. doi:10.1063/5.0004835

44. Nosé S. A molecular dynamics method for simulations in the canonical ensemble. *Mol Phys*. 1984;52(2):255-268. doi:10.1080/00268978400101201

45. Hoover WG. Canonical dynamics: equilibrium phase-space distributions. *Phys Rev A*. 1985;31(3):1695-1697. doi:10.1103/PhysRevA.31.1695

46. Scalmani G, Frisch MJ. Continuous surface charge polarizable continuum models of solvation. I. General formalism. *J Chem Phys*. 2010;132(11):114110. doi:10.1063/1.3359469

47. Head-Gordon M, Pople JA, Frisch MJ. MP2 energy evaluation by direct methods. *Chem Phys Lett*. 1988;153(6):503-506. doi:10.1016/0009-2614(88)85250-3

48. Ditchfield R, Hehre WJ, Pople JA. Self-consistent molecular-orbital methods. IX. An extended Gaussian-type basis for molecular-orbital studies of organic molecules. *J Chem Phys*. 1971;54(2):724-728. doi:10.1063/1.1674902

49. Frisch MJ, Trucks GW, Schlegel HB, et al. *Gaussian 16, Revision C.01*. Gaussian, Inc; 2016.

50. McCall MJ, Gulson B, Andrews D. Consumer use of sunscreens containing nanoparticles. *Nanotechnology Environmental Health and Safety*. Elsevier; 2018:389-423.

51. Mayerhöfer TG, Pahlow S, Popp J. The Bouguer-beer-Lambert law: shining light on the obscure. *ChemPhysChem*. 2020;21(18):2029-2046. doi:10.1002/cphc.202000464

52. Gonzalez H, Tarras-Wahlberg N, Strömdahl B, et al. Photostability of commercial sunscreens upon sun exposure and irradiation by ultraviolet lamps. *BMC Dermatol*. 2007;7(1):1. doi:10.1186/1471-5945-7-1

53. Hojerová J, Medovcíková A, Mikula M. Photoprotective efficacy and Photostability of fifteen sunscreen products having the same label SPF subjected to natural sunlight. *Int J Pharm*. 2011;408(1–2):27-38. doi:10.1016/j.ijpharm.2011.01.040

SUPPORTING INFORMATION

Additional supporting information can be found online in the Supporting Information section at the end of this article.